Image Fusion Method Based on Directional Contrast-Inspired Unit-Linking Pulse Coupled Neural Networks in Contourlet Domain

Xi Cai
Northeastern University at Qinhuangdao, Qinhuangdao, China
Email: cicy_2001@163.com

Guang Han
College of Information Science and Engineering, Northeastern University, Shenyang, China
Email: a00152738@sohu.com

Jinkuan Wang*
Northeastern University at Qinhuangdao, Qinhuangdao, China
Email: wjk@mail.neuq.edu.cn

***Abstract*—To take full advantage of global features of source images, we propose an image fusion method based on adaptive unit-linking pulse coupled neural networks (ULPCNNs) in the contourlet domain. Considering that each high-frequency subband after the contourlet decomposition has rich directional information, we employ directional contrast of each coefficient as the external stimulus to inspire each neuron. Linking range is also related to the contrast in order to adaptively improve the global coupling characteristics of ULPCNNs. In this way, biological activity of human visual systems to detailed information of images can be simulated by the output pulses of the ULPCNNs. The first firing time of each neuron is utilized to determine the fusion rule for corresponding detailed coefficients. Experimental results indicate the superiority of our proposed algorithm, for multifocus images, remote sensing images, and infrared and visible images, in terms of visual effects and objective evaluations.**

***Index Terms*—Image fusion, contourlet transform, unit-linking pulse coupled neural network**

I. INTRODUCTION

Owing to widespread use of multisensor systems, much research has been invested to develop the technology of image fusion. Ordinarily, 2-D image fusion is to merge complementary information from multiple images of the same scene, and obtain one single image of better quality [1]-[4]. This promotes its increasingly extensive application in digital camera imaging, battlefield surveillance and remote sensing. As a major class of image fusion methods, the ones based on multiscale decomposition (MSD) take into account the sensitivity of human visual system (HVS) to detailed information, and hence receive better fusion results than other methods [5][6]. To improve the performance, MSD transforms and fusion rules have become the main focus in the fusion methods based on MSD [7]-[9].

Typically, MSD transforms include: pyramid transform, wavelet transform, curvelet transform, etc. With further development of MSD theory, a superior two-dimensional representation, contourlet transform was exploited to overcome limitations of traditional MSD transforms [10]. Its characteristics of multidirection and anisotropy make it sensitive to directions and sparse while representing objects with edges. Especially, contourlet transform allows for different and flexible number of directions at each scale, and hence can capture detailed information in any arbitrary direction. These advantages make the contourlet transform quite attractive to image fusion [11]-[14]. In most contourlet-based fusion methods, researchers adopt fusion rules to choose more salient high-frequency information, for example, [12] and [13] respectively chose the coefficient with the maximum region energy and the maximum edge information.

However, the traditional fusion rules could not make good use of global features of images, for they were most based on features of a single pixel or local regions. In our study, we present a bio-inspired salience measure based on unit-linking pulse coupled neural networks (ULPCNNs), and capture the global features of source images by using the global coupling properties of the ULPCNNs. PCNN originated from the experimental observations of synchronous pulse bursts in cat visual cortex [15], and is capable to simulate biological activity of HVS; ULPCNN is a simplified version of the basic PCNN with fewer parameters [16]. When motivated by external stimuli from images, ULPCNNs can generate series of binary pulses containing much information of features such as edges, textures, etc.

* Corresponding author.

doi:10.4304/jcp.8.6.1544-1551

In this paper, we propose an image fusion method based on directional contrast-stimulated ULPCNNs with adaptive linking range in the contourlet domain (CT-ULPCNN). ULPCNN neurons are inspired by directional contrast revealing the prominence of each directional subband, and such a ULPCNN is expected to possess good sensitivity to directional information of objects in images. The linking range is also determined by corresponding directional contrast. In this way, the global coupling character of the ULPCNN is better represented than that with constant linking range, especially for the strong stimulus. In our fusion rules, the first firing time of each neuron is chosen as the salience measure. Experimental results suggested that CT-ULPCNN has better fusion results for multifocus images, remote sensing images, and infrared and visible images, which actually proves the advantages of the proposed method capturing the prominent directional features of each subband in the contourlet domain.

The outline of the rest of the paper is as follows. Contourlet transform is briefly introduced in Section II. In Section Ⅲ, we describe the theories of basic PCNN and ULPCNN, respectively. Detailed procedure of CT-ULPCNN algorithm is proposed in Section Ⅳ, and its effectiveness is certified and analyzed in Section Ⅴ. Finally, conclusion is drawn in Section Ⅵ.

II. CONTOURLET TRANSFORM

Contourlet transform is a multi-scale and multi-directional transform. It was initially developed in discrete domain, and hence easy for digital implementation. Contourlet transform combines Laplacian Pyramid (LP) and Directional Filter Bank (DFB) into a double filter bank structure, so it is also called Pyramidal Direction Filter Bank (PDFB). In essence, LP is first executed to capture the point discontinuities, and then followed by DFB to link point discontinuities into linear structures. Fig. 1 shows the contourlet decomposition in the frequency domain, where shaded parts denote the support regions of corresponding filters. During the contourlet decomposition, an image is first decomposed by LP into a low-frequency subband and mutiple high-frequency subbands, and then each high-frequency subband is fed into DFB to generate multiple directional subbands.

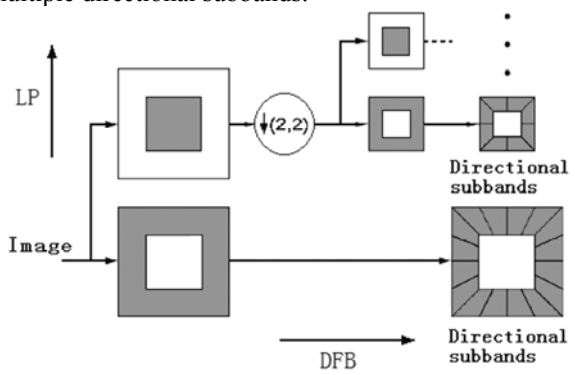

Figure 1. Frame of contourlet decomposition in the frequency domain.

In the contourlet transform, the number of directional subbands in each scale is usually $2^n (n \in N)$ and quite flexible when n is set differently. Therefore, the contourlet transform is able to provide detailed information in any arbitrary direction, which is its major advantage over the other MSD transforms. Meanwhile, after the contourlet decomposition, majority of the contourlet coefficients of an image are close to zero, concentrating the most information and energy, which indicates the sparsity of the contourlet transform.

III. PCNN AND ULPCNN

A. Basic PCNN

PCNN is a feedback network in a single layer with neurons laterally interconnected, which can imitate the biological characteristics of HVS. Basically, each neuron consists of a receptive field, a modulation product and a pulse generator. For the neuron located at (i, j) in a PCNN, the receptive field involves a linking input L_{ij} and a feeding input F_{ij} ; The modulation product combines F_{ij} with the biased L_{ij} to form a total internal activity U_{ij} ; The generator Y_{ij} will produce a pulse (i.e. firing) if U_{ij} exceeds the dynamic threshold θ_{ij} . When inspired by external stimulus S_{ij} and influenced by signals from neighboring neurons $\{Y_{kl}\}$, the discrete mathematical equations for F_{ij} , L_{ij} , U_{ij} , Y_{ij} and θ_{ij} can be described as follows.

$$F_{ij}(n) = e^{-\alpha_F} F_{ij}(n-1) + V_F \sum_{kl} M_{ijkl} Y_{kl}(n-1) + S_{ij}, \quad (1)$$

$$L_{ij}(n) = e^{-\alpha_L} L_{ij}(n-1) + V_L \sum_{kl} W_{ijkl} Y_{kl}(n-1), \quad (2)$$

$$U_{ij}(n) = F_{ij}(n) \cdot (1 + \beta L_{ij}(n)), \quad (3)$$

$$Y_{ij}(n) = \begin{cases} 1, & U_{ij}(n) > \theta_{ij}(n-1), \\ 0, & \text{otherwise}, \end{cases} \quad (4)$$

$$\theta_{ij}(n) = e^{-\alpha_\theta} \theta_{ij}(n-1) + V_\theta Y_{ij}(n). \quad (5)$$

Fig. 2 illustrates the basic model for a single neuron located at (i, j) in a PCNN. Output pulses of neurons in the $k \times l$ neighborhood centered at (i, j) enter into the neuron at (i, j) and then influence its next output, where $k \times l$ is called linking range. L_{ij} receives pulses from surrounding neurons ((2)), and F_{ij} receives not only the neighboring signals but also the external stimulus S_{ij}

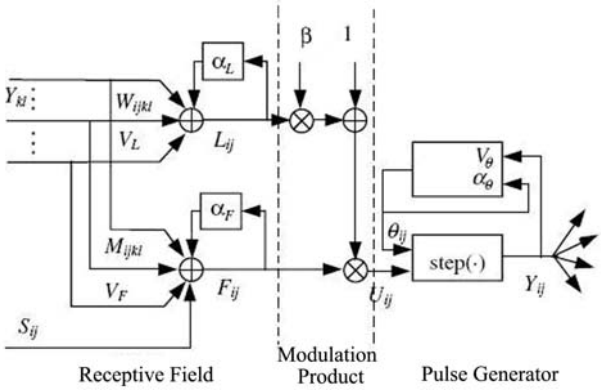

Figure 2. Basic model for a single PCNN neuron.

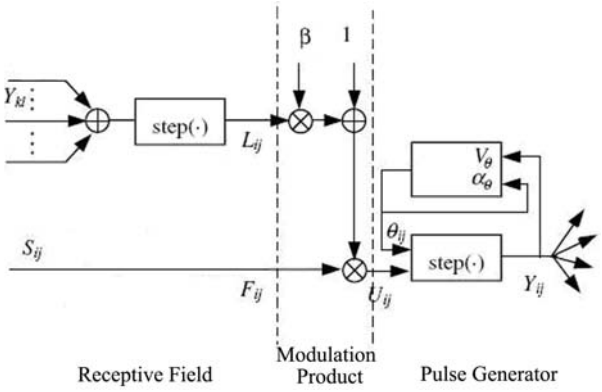

Figure 3. Simplified model for a single ULPCNN neuron.

((1)). U_{ij} is obtained by multiplying F_{ij} with the biased L_{ij} ((3)). If U_{ij} is above the neuromime threshold θ_{ij}, Y_{ij} will generate a pulse ((4)), and simultaneously θ_{ij} will increase enormously ((5)) to block another pulse in the next iteration. Without an output pulse, θ_{ij} would decay exponentially ((5)), until it drops below the internal activity and at that time a pulse will be outputted again. In this way, these processes run over and over again. In (1)-(5), n denotes the iteration times; α_F, α_L, α_θ and V_F, V_L, V_θ are attenuation time constants and inherent voltage potential of F_{ij}, L_{ij} and θ_{ij}, respectively; M_{ijkl} and W_{ijkl} signify synaptic weight strength for F_{ij} and L_{ij}; β indicates linking strength determining contribution of the linking input to the internal activity.

B. ULPCNN

PCNN is qualified to imitate the biological features of HSV and hence apply to image processing [17]-[19]; however, so many parameters in the model should be set during use. So far, the relation between model parameters and network outputs is still ambiguous, and it is really difficult to determine the proper PCNN parameters. Therefore, ULPCNN is presented to simplify the PCNN by means of decreasing parameters and making the linking inputs of ULPCNN neurons uniform [16]. Fig. 3 displays the simplified model for a single ULPCNN neuron. The processes of a single ULPCNN neuron are displayed as

$$F_{ij}(n) = S_{ij}, \tag{6}$$

$$L_{ij}(n) = \begin{cases} 1, & \sum_{kl} Y_{kl}(n-1) > 0, \\ 0, & \text{otherwise}, \end{cases} \tag{7}$$

$$U_{ij}(n) = F_{ij}(n) \cdot (1 + \beta L_{ij}(n)), \tag{8}$$

$$Y_{ij}(n) = \begin{cases} 1, & U_{ij}(n) > \theta_{ij}(n-1), \\ 0, & \text{otherwise}, \end{cases} \tag{9}$$

$$\theta_{ij}(n) = e^{-\alpha_\theta}\theta_{ij}(n-1) + V_\theta Y_{ij}(n). \tag{10}$$

According to (7), if any neuron in the $k \times l$ neighborhood fires, L_{ij} will have a unity input, and then the centered neuron will be encouraged to fire. Obviously, impulse expanding behavior is much clearer and more controllable with much fewer parameters than the basic PCNN.

IV. The Proposed Image Fusion Method

Considering that HVS is very sensitive to detailed information, researchers commonly employ fusion rules to choose more significant information in high-frequency subbands. In our study, we provide a new image fusion method based on directional contrast-inspired ULPCNN in the contourlet domain. Directional features are fed into ULPCNN to imitate the biological activity of HSV, and then transmitted in the form of pulses. The linking range for each neuron is adaptive to corresponding directional contrast. The first firing time of each neuron is used to determine the decision in fusion rules. Because of the global coupling characters of the ULPCNNs, global features of images can be made good use of during fusion in our proposed method.

Fig. 4 shows the flowsheet of our proposed method. Detailed procedure of the CT-ULPCNN method is given as follows.

- Source images *A* and *B* are decomposed by the contourlet transform to coefficients $\{a_R^A, d_{r,p}^A\}$ and $\{a_R^B, d_{r,p}^B\}$, respectively. Denote the coefficients of the fused image *F* by $\{a_R^F, d_{r,p}^F\}$. Here, *R* is the decomposition level, a_R^X (*X*=*A*,*B*,*F*) denotes the coefficients in the low-frequency subband of image *X*, and $d_{r,p}^X$ (*X*=*A*,*B*,*F*) denotes the

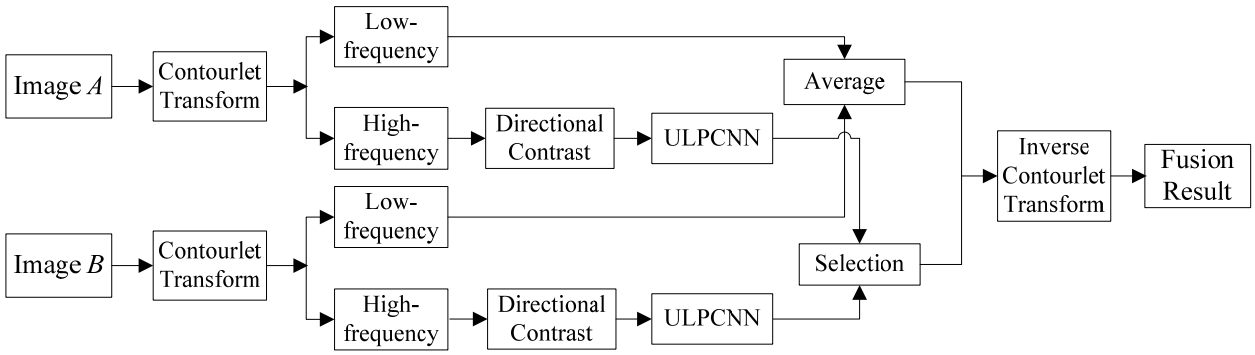

Figure 4. Flowsheet of our proposed method.

coefficients in the *p*th directional subband at the *r*th $(1 \le r \le R)$ scale of image *X*.

- In each directional subband, directional contrast at location (i, j) can be calculated as

$$Ctr_{r,p}^{X}(i,j) = \left| d_{r,p}^{X}(i,j) \Big/ a_{r}^{X}(u,v) \right|. \qquad (11)$$

where a_r^X indicates the low-frequency subband at the *r*th scale of image *X*, and the coarse coefficient at location (u,v) corresponds to the same region as $d_{r,p}^X(i,j)$ does. Then $Ctr_{r,p}^X(i,j)$ is imported as the external stimulus S_{ij} into the ULPCNN neuron located at (i,j). Its linking range is fixed according to

$$k_{ij} \text{ or } l_{ij} = \begin{cases} 5, & Ctr_{r,p}^{X}(i,j) \ge \max(Ctr_{r,p}^{X}) \Big/ 2, \\ 3, & \text{otherwise.} \end{cases} \qquad (12)$$

The ULPCNN operates iteratively as (6)-(10), until all neurons are fired at least once. The first firing time of the neuron at location (i,j) in the *p*th directional subband at the *r*th scale of image *X* should be recorded as $T_{r,p}^X(i,j)$ (*X*=*A*,*B*).

- $\{a_R^F, d_{r,p}^F\}$ are obtained by the following rules.

For the low-frequency,

$$a_R^F(i,j) = \left(a_R^A(i,j) + a_R^B(i,j) \right) \Big/ 2, \qquad (13)$$

For the high-frequency,

$$d_{r,p}^F(i,j) = \begin{cases} d_{r,p}^A(i,j), & T_{r,p}^A(i,j) < T_{r,p}^B(i,j), \\ d_{r,p}^B(i,j), & \text{otherwise.} \end{cases} \qquad (14)$$

- The fused image *F* is finally achieved via contourlet reconstruction from $\{a_R^F, d_{r,p}^F\}$.

V. Experimental Results

To certify the effectiveness of our proposed method, we have performed the CT-ULPCNN method on many pairs of images. Considering limitation of space, we take three pairs of images (shown in Fig. 5) as examples to provide the experimental results. Fig. 5(a) is a pair of multifocus images focusing on different objects of the same scene, Fig. 5(b) displays a pair of remote sensing images taken from different wavebands, and Fig. 5(c) is a pair of infrared and visible images.

In this section, following two sets of tests are designed to prove the validity of our proposed method. In ***Test 1***, we highlight the advantage of the adaptive ULPCNNs model in our proposed method by comparing its behavior to three existing contourlet-based image fusion algorithms, including CT-Miao [12], CT-Zheng [13], and CT-Yang [14]. ***Test 2*** demonstrates the prominence of the CT-ULPCNN method by its comparison with some typical MSD-based image fusion methods, namely, the gradient pyramid-based method (Gradient) [20], the conventional discrete wavelet transform-based method (DWT) [21], the curvelet transform-based method (Curvelet) [22], and the nonsubsampled contourlet transform-based method (NSCT) [23].

In our experiments, images were all decomposed into four levels in use of the above MSD-based fusion methods. Especially, for the contourlet-based image fusion methods, the decomposed four scales were divided into 4, 4, 8, and 16 directional subbands from coarse to fine scales, respectively. Furthermore, in our proposed method, parameters were set as $\alpha_\theta = 0.5$, $V_\theta = 20$ and $\beta = 3$.

A. Test 1

Fig. 6-Fig. 8, respectively, provide the fusion results of *pepsi*, *remote* and *camp* using the CT-ULPCNN, CT-Miao, CT-Zheng, and CT-Yang methods. To show more clearly, we select a section of each result to enlarge.

As can be seen from Fig. 6, for multifocus images, the CT-Miao, CT-Zheng, and CT-Yang methods all have the problem of ring artifacts in their fusion results, and the partial result of the CT-Zheng has the severest ghost image even with a post-processing of consistency verification (CV) to intentionally reduce the ringing artifacts; whereas our proposed method possesses a result with the fewest ringing artifacts, highest contrast and finest details without the CV.

As seen from Fig. 7, the CT-ULPCNN method still has the best performance with the smoothest surface in the flat regions. However, the result of the CT-Yang

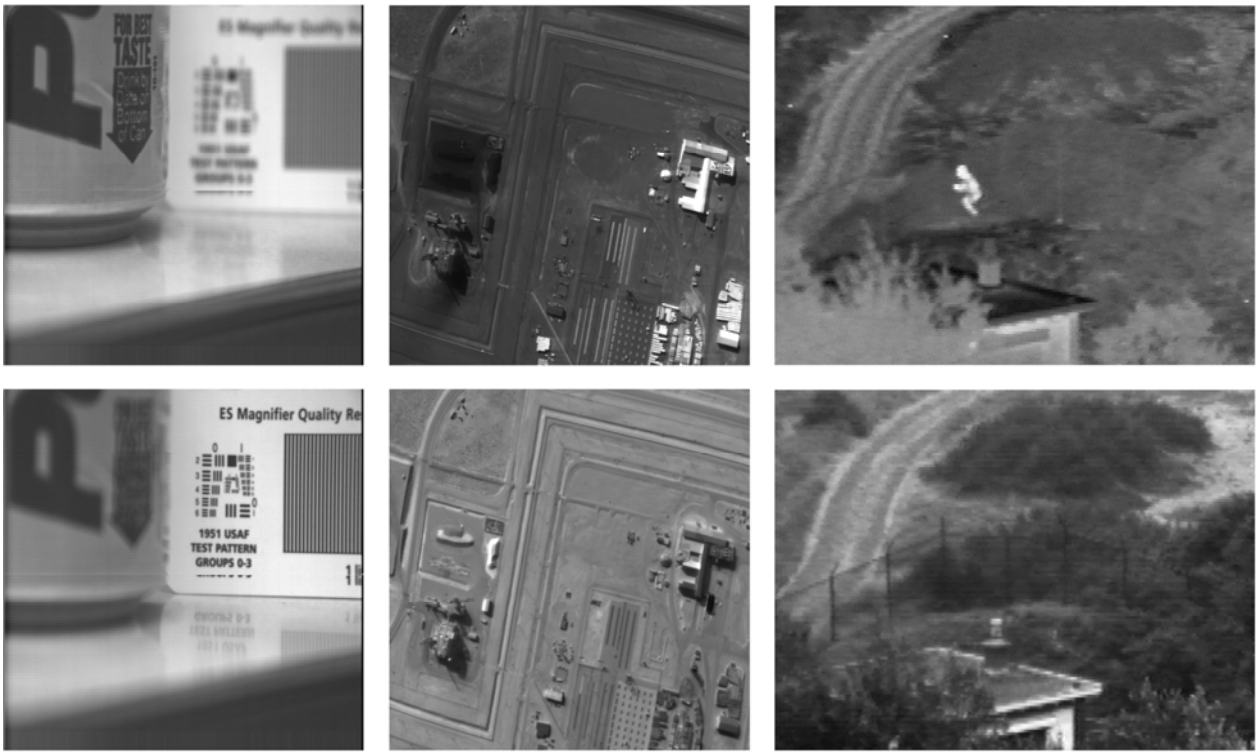

(a) (b) (c)

Figure 5. Three pairs of test images: (a) *pepsi*, (b) *remote* and (c) *camp*.

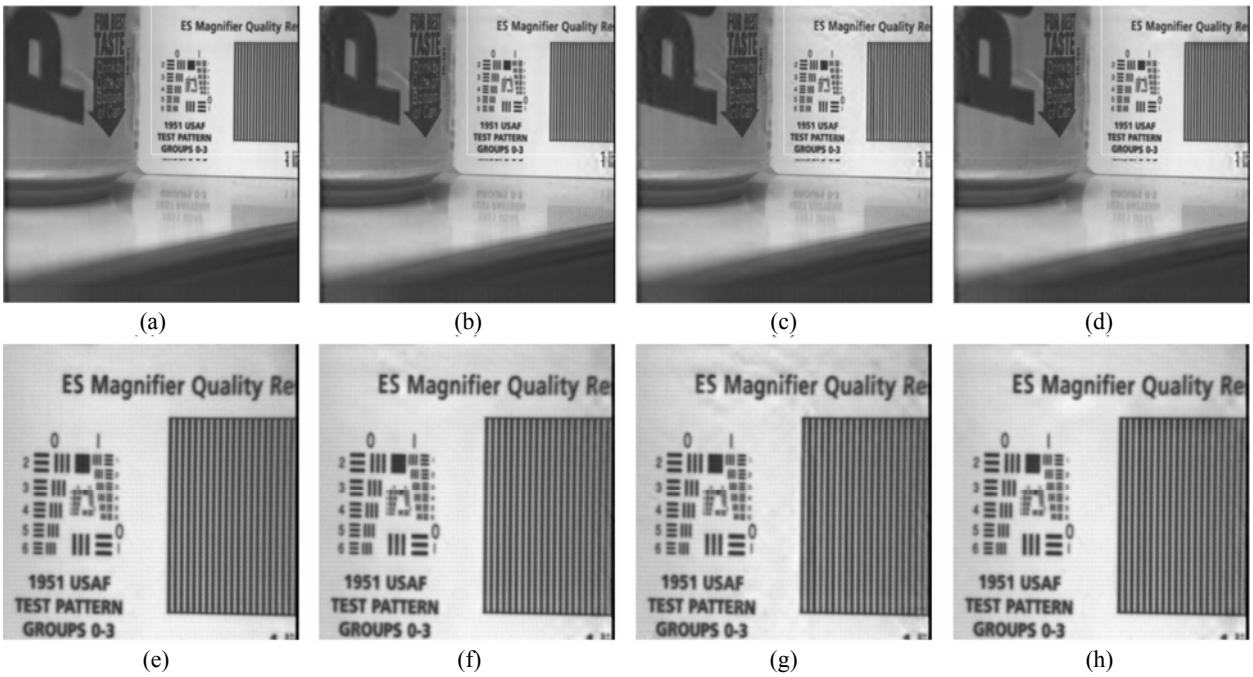

(a) (b) (c) (d)

(e) (f) (g) (h)

Figure 6. Fusion results of *pepsi*: (a) our method, (b) CT-Miao, (c) CT-Zheng, (d) CT-Yang, and (e)-(h) are partial enlargements of (a)-(d), respectively.

method is visually unsatisfactory. This is because the fusion rule of the CT-Yang method for the low-frequency subband is to choose the low-frequency coefficient with the maximum region variance, and such a rule makes the fused approximated image unsmooth when applying to source images with distinct basic illuminations, such as remote sensing images in different wavebands.

Likewise, for the pair of infrared and visible images, the CT-Yang method generates the worst fusion result; whereas the hot target (i.e. the man) is the most distinguishable in the result of our proposed method (Fig. 8(a)).

Obviously, the CT-ULPCNN achieves superior visual quality over the other three contourlet-based fusion methods.

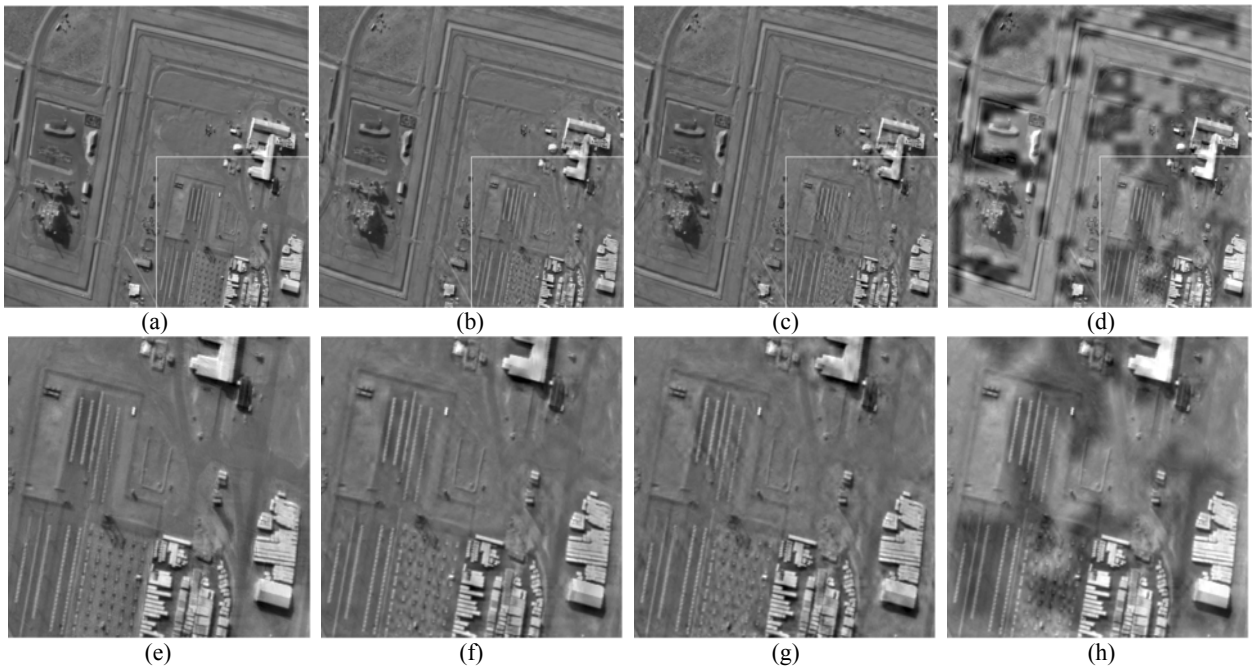

Figure 7. Fusion results of *remote*: (a) our method, (b) CT-Miao, (c) CT-Zheng, (d) CT-Yang, and (e)-(h) are partial enlargements of (a)-(d), respectively.

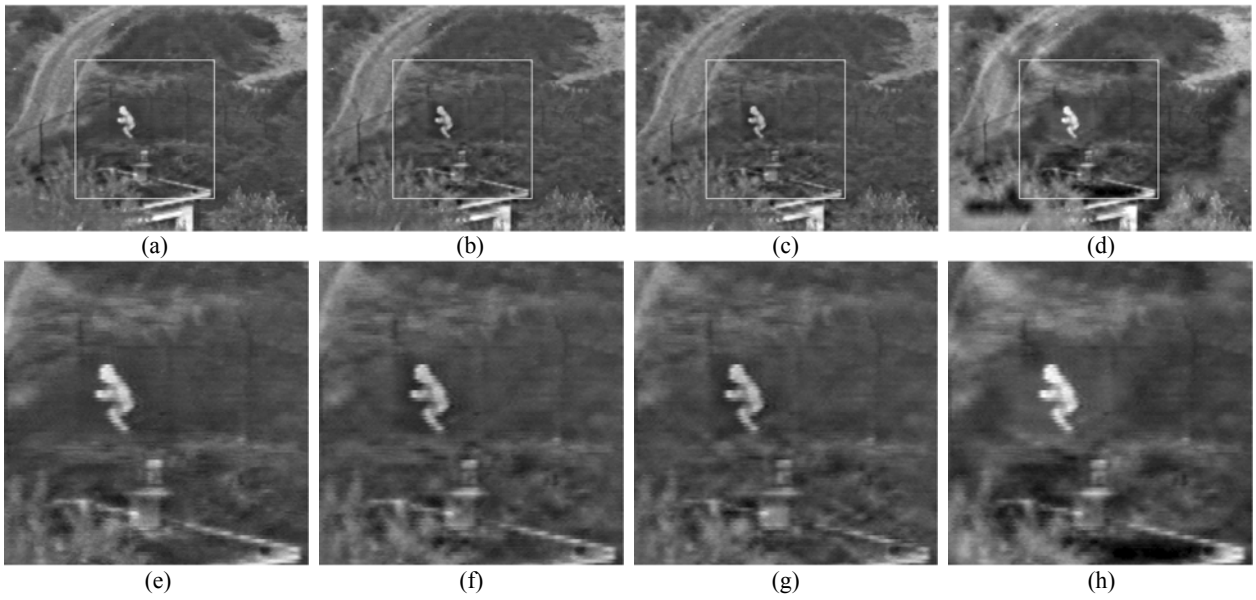

Figure 8. Fusion results of *camp*: (a) our method, (b) CT-Miao, (c) CT-Zheng, (d) CT-Yang, and (e)-(h) are partial enlargements of (a)-(d), respectively.

To evaluate the fusion effects more objectively, we introduce average gradient (AG), spatial frequency (SF), mutual information (MI), $Q^{AB/F}$ [24] and a universal image quality index (UIQI) [25] as fusion indices. Generally, the larger the above five objective indices, the better the fusion result is.

Table Ⅰ-Ⅲ show the indices for fusion results of the three pairs of images in Fig. 5, respectively. According to these tables, the results of our method always have the largest values in the average gradient, spatial frequency, mutual information, $Q^{AB/F}$ and the universal image quality index, no matter for the pair of multifocus images, or the pair of remote sensing images, or the pair of infrared and visible images. This clearly proves the superiority of our proposed method on the objective evaluations.

B. Test 2

We also make a comprehensive comparison of our proposed method with other four classical MSD-based fusion methods, including the Gradient [20], DWT [21], Curvelet [22] and NSCT [23].

Because of the limitations of space, we only exhibit the fusion results of *pepsi* in Fig. 9. Apparently, the result of the Gradient method has the lowest contrast, and the Curvelet and the NSCT methods also generate

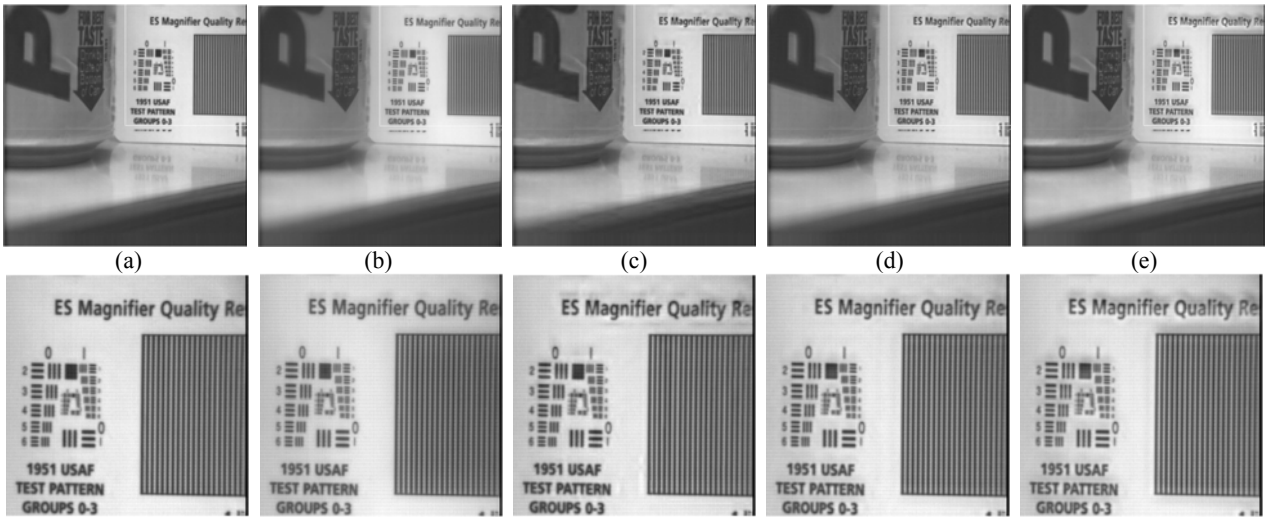

Figure 9. Fusion results of *pepsi*: (a) our method, (b) Gradient, (c) DWT, (d) Curvelet, (e) NSCT and (f)-(j) are partial enlargements of (a)-(e), respectively.

results with relatively lower contrast, and the results of the NSCT and especially the DWT methods have heavy ringing artifacts; whereas our proposed method produces a result with the highest contrast and the fewest ringing artifacts. Visually, the advantage of our proposed method is prominent.

Table Ⅳ shows the fusion indices of results by using the above five image fusion methods for *pepsi*. The result of our proposed method has the largest mutual information, $Q^{AB/F}$, and the universal image quality index, except that, it has lower average gradient and spatial frequency than those of the DWT and the NSCT methods. This is because that, for *pepsi*, severe ringing artifacts in the results of the DWT (Fig. 9(h)) and the NSCT (Fig. 9(j)) may cause larger values in the average gradient and the spatial frequency.

Experimental results demonstrate that, the superiority of the proposed method, in the field of visual quality and objective evaluations, is prominent. This mainly benefits from the global coupling characteristics of the ULPCNNs model. By using the features extracted from the output pulses of the ULPCNNs, the biological activity of the HVS to detailed information of images can be reflected very well.

VI. Conclusion

In this paper, we provide a new image fusion algorithm based on the ULPCNNs in the contourlet domain. Directional contrast is fed into the ULPCNNs to imitate the biological activity of HVS to directional information. Linking range is also determined by the contrast, flexibly making good use of global features of images. Experimental results illuminate that, the CT-ULPCNN method outperforms the other methods in both the visual and the objective fields.

Acknowledgment

This work was supported by the Fundamental Research Funds for the Central Universities (N110323004) and the Natural Science Foundation of Hebei Province under Grant No.F2012501001.

TABLE I.

Fusion Indices for *pepsi*

Method	Metrics				
	AG	SF	MI	$Q^{AB/F}$	UIQI
CT-ULPCNN	5.6722	13.986	6.7704	0.74015	0.89467
CT-Miao	5.5759	13.923	6.4653	0.73644	0.85769
CT-Zheng	5.4912	13.833	6.2256	0.71153	0.84454
CT-Yang	5.5684	13.933	6.4987	0.73185	0.85492

TABLE II.

Fusion Indices for *REMOTE*

Method	Metrics				
	AG	SF	MI	$Q^{AB/F}$	UIQI
CT-ULPCNN	7.0993	15.362	1.6673	0.56055	0.69729
CT-Miao	6.6244	14.646	1.4599	0.53364	0.64608
CT-Zheng	6.6965	14.526	1.4182	0.49636	0.63166
CT-Yang	7.0883	15.037	1.1027	0.46923	0.50629

TABLE III.

Fusion Indices for *CAMP*

Method	Metrics				
	AG	SF	MI	$Q^{AB/F}$	UIQI
CT-ULPCNN	7.2227	13.506	1.5600	0.46466	0.63175
CT-Miao	6.8137	12.747	1.3814	0.4067	0.56411
CT-Zheng	6.7682	12.529	1.3594	0.38244	0.55494
CT-Yang	7.0183	13.064	1.5026	0.38959	0.51602

TABLE IV.

Fusion Indices for *PEPSI*

Method	Metrics				
	AG	SF	MI	$Q^{AB/F}$	UIQI
CT-ULPCNN	5.6722	13.986	6.7704	0.74015	0.89467
Gradient	4.7795	11.987	6.135	0.73947	0.88898
DWT	5.8093	14.173	6.3616	0.72958	0.86539
Curvelet	5.6215	13.977	6.5344	0.73633	0.88186
NSCT	7.7004	18.99	6.7607	0.68791	0.78435

REFERENCES

[1] Y. F. Li, X. Y. Feng, and Y. Fan, "Investigation of Shift Dependency Effects on Multiresolution-Based Image Fusion Performance," *Journal of Software.*, vol. 6, no. 3, pp. 475–482, March 2011.

[2] X. B. Jin, J. Bao, and J. J. Du, "Image Enhancement Based on Selective - Retinex Fusion Algorithm," *Journal of Software*, vol. 7, no. 6, pp. 1187–1194, June 2012.

[3] M. Xu, H. Chen, and P. K. Varshney, "An image fusion approach based on Markov random fields," *IEEE Trans. Geosci. Remote Sens.*, vol. 49, pp. 5116–5127, December 2011.

[4] W. Yao and M. Han, "Improved GIHSA for image fusion based on parameter optimization," *Int. J. Remote Sens.*, vol. 31, pp. 2717–2728, 2010.

[5] Z. Zhang and R. S. Blum, "A categorization of multiscale-decomposition-based image fusion schems with a performance study for a digital camera application," *Proc. IEEE*, vol. 87, pp. 1315–1326, August 1999.

[6] S. Li, B. Yang, and J. Hu, "Performance comparison of different multi-resolution transforms for image fusion," *Inf. Fusion*, vol. 12, pp. 74–84, April 2011.

[7] X. Cai and G. Han, "Improved Statistical Image Fusion Method Using a Continuous-Valued Blur Factor," *Opt. Eng.*, vol. 51, pp. 047004-1–047004-10, 2012.

[8] M. Chandana, S. Amutha, and N. Kumar, "A Hybrid Multi-focus Medical Image Fusion Based on Wavelet Transform," *Int. J. Res. Rev. Comput. Sci.*, vol. 2, pp. 948–953, August 2011.

[9] B. Zhang, "Study on image fusion based on different fusion rules of wavelet transform," in *3rd Int. Conf. Adv. Comput. Theory Eng.,Proc.*, 2010, pp. 649–653.

[10] M. N. Do and M. Vetterli, "The Contourlet Transform: An Efficient Directional Multiresolution Image Representation," *IEEE Trans. Image Process.*, vol. 14, pp. 2091–2106, December 2005.

[11] X. Cai and W. Zhao, "Discussion upon Effects of Contourlet Lowpass Filter on Contourlet-Based Image Fusion Algorithms," *Acta Autom. Sin.*, vol. 35, pp. 258–266, March 2009.

[12] Q. G. Miao and B. S. Wang, "A Novel Image Fusion Method Using Contourlet Transform," in *IEEE Int. Conf. Commun. Circuits Sys.*, 2006, pp. 548–552.

[13] Y. A. Zheng, C. S. Zhu, J. S. Song, and X. H. Zhao, "Fusion of Multi-band SAR Images Based on Contourlet Transform." in *IEEE Int. Conf. on Inf. Acquis.*, 2006, pp. 420–424.

[14] L. Yang, B. L. Guo, and W. Ni, "Multifocus Image Fusion Algorithm Based on Region Statistics in Contourlet Domain," *J. Xi'an Jiaotong Univ.*, vol. 41, pp. 448–452, April 2007.

[15] Z. B. Wang, Y. D. Ma, F. Y. Cheng, and L. Z. Yang, "Review of Pulse-Coupled Neural Networks," *Image Vis. Comput.*, vol. 28, pp. 5–13, January 2010.

[16] X. D. Gu, "A New Approach to Image Authentication using Local Image Icon of Unit-linking PCNN," in *IEEE Int. Conf. Neural. Netw.*, 2006, pp. 1036–1041.

[17] S. Wei, Q. Hong, and M. S. Hou, "Automatic image segmentation based on PCNN with adaptive threshold time constant," *Neurocomput.*, vol. 74, pp. 1485–1491, April 2011.

[18] J. C. Fu, C. C. Chen, J. W. Chai, S. T. C. Wong, and I. C. Li, "Image segmentation by EM-based adaptive pulse coupled neural networks in brain magnetic resonance imaging," *Comput. Med. Imaging Graph.*, vol. 34, pp. 308–320, June 2010.

[19] D. Agrawal and J. Singhai, "Multifocus image fusion using modified pulse coupled neural network for improved image quality," *IET Image Process.*, vol. 4, pp. 443–451, December 2010.

[20] P. J. Burt and R. J. Kolczynski, "Enhanced image capture through fusion," in *Proc. of 4th Int. Conf. Comput. Vision*, 1993, pp. 173–182.

[21] F. Hassainia, M. I. Magana, F. Langevin, and J. P. Kernevez, "Image fusion by an orthogonal wavelet transform and comparison with other methods," in *14th Annu. Int. Conf. IEEE*, 1992, pp. 1246–1247.

[22] H. H. Li, L. Guo, and H. Liu, "Research on image fusion based on the second generation curvelet transform," *Acta Opt. Sin.*, vol. 26, pp. 657–662, May 2006.

[23] X. B. Qu, G. F. Xie, J. W. Yan, Z. Q. Zhu, and B. G. Chen, "Image fusion algorithm based on neighbors and cousins information in nonsubsampled contourlet transform domain," in *Proc. Int. Conf. Wavelet Anal. Pattern Recognit.*, 2007, pp. 1797−1802.

[24] V. Petrovic and C. S. Xydeas, "Objective evaluation of signal-level image fusion performance," *Opt. Eng.*, vol. 44, pp. 087003-1–087003-8, August 2005.

[25] G. Piella and H. Heijmans, "A New Quality Metric for Image Fusion," in *IEEE Int. Conf. Image Process.*, 2003, pp. 173−176.

Xi Cai received her B.S. and Ph.D. degrees from the School of Electronic and Information Engineering, Beihang University, China, in 2005 and 2011, respectively. Now she is a teacher at Engineering Optimization and Smart Antenna Institute, Northeastern University at Qinhuangdao, China. Her research interests include image fusion, image registration and object detection.

Guang Han received his B. Eng. and M. Eng. degrees from the School of Electronic and Information Engineering, Beihang University, China, in 2005 and 2008, respectively. Now he is a Ph.D. candidate at College of Information Science and Engineering, Northeastern University. His research interests include object detection and object tracking based on video sequences.

Jinkuan Wang received the M.Eng. degree from Northeastern University, Shenyang, China, in 1985, and the Ph.D. degree from the University of Electro-Communications, Chofu, Japan, in 1993.

In 1990, he joined the Institute of Space and Astronautical Science, Sagamihara, Japan, as a special member. He was an Engineer with the Research Department, COSEL Company, in 1994. He is currently the President of the Northeastern University at Qinhuangdao, Hebei, China, where he has been a Professor since 1998. He has been a main researcher in several National Natural Science Foundation research projects of China. His main interests are in the areas of intelligent control, adaptive array, wireless sensor networks and image processing.